STAR NDSI collection: A cloud-free MODIS NDSI dataset (2001– 2020) for China

Yinghong Jing[1], Xinghua Li[2], and Huanfeng Shen[1,3]

[1]School of Resource and Environmental Sciences, Wuhan University, Wuhan 430079, China

5   [2]School of Remote Sensing and Information Engineering, Wuhan University, Wuhan 430079, China

[3]Collaborative Innovation Centre of Geospatial Technology, Wuhan 430079, China

Correspondence to: Xinghua Li (lixinghua5540@whu.edu.cn), Huanfeng Shen (shenhf@whu.edu.cn)

Abstract. Snow dynamics are crucial in ecosystems, affecting radiation balance, hydrological cycles, biodiversity, and human activities. Snow areas with notably diverse characteristics are extensively distributed in China, mainly including Northern

10   Xinjiang (XJ), Northeast China (NC), and Tibetan Plateau (TP). Spatio-temporal continuous snow monitoring is indispensable for ecosystem maintenance. Nevertheless, the formidable challenge of cloud obscuration severely impedes data collection. In the past decades, abundant binary snow cover area (SCA) maps have been retrieved from moderate resolution imaging spectroradiometer (MODIS) datasets. However, the integrated normalized difference snow index (NDSI) maps containing additional details on snow cover extent are still extremely scarce. In this study, a recent 20-year stretch seamless MODIS NDSI

15   collection in China is generated for the first time using a Spatio-Temporal Adaptive fusion method with erroR correction (STAR), which comprehensively considers spatial and temporal contextual information. Evaluation tests confirm that the gap-filled STAR NDSI collection is highly consistent with the Landsat NDSI dataset, with an average correlation coefficient of approximately 0.84. Consequently, this collection can serve as a basic dataset for hydrological and climatic modeling to explore various critical environmental issues. This collection is available from https://doi.org/10.5281/zenodo.5644386 (Jing

20   et al., 2021).

1 Introduction

Snow is a fundamental component of the cryosphere, strongly interacting with global energy budgets and hydrological dynamics (Hall et al., 1995). Snow cover has a remarkable impact on the Earth's radiation balance due to its highly reflective nature, thus generating feedbacks in the global climate system (Konzelmann and Ohmura, 1995). Up to one-sixth of the world's

25   population relies on meltwater from glaciers and snowpacks for drinking, irrigation, hydropower generation, and industrial production (Barnett et al., 2005). Therefore, snow dynamics have a profound impact on climate change and human activities. The snow cover extent of the northern hemisphere has continued to decrease since the mid-20th century (Pachauri and Meyer, 2014). However, regional-scale snow variations in different environmental conditions present mixed trends due to the strong sensitivity of snow cover to climate change (Bormann et al., 2018). The snow cover regions in China are extensively distributed

30   with remarkable spatial and temporal heterogeneity (Wang et al., 2018), mainly in Northern Xinjiang (XJ), Northeast China

(NC), and Tibetan Plateau (TP). Therefore, accurate snow cover acquisition in China is significant for snow pattern analysis, water resource management, and climate change monitoring, etc.

China has conducted large-scale observations of snow parameters since the 1950s through meteorological stations, providing a valuable data basis for long-term snow-related studies. However, accurately depicting the snow characteristics in
35   China, especially on TP dominated by patchy and shallow snow, is difficult due to the sparsely and unevenly distributed traditional in-situ observations. Satellite-based remote sensing is a prominent alternative for continuous snow cover monitoring at meso and macro scales. Moderate resolution imaging spectroradiometer (MODIS) snow cover datasets are extensively used for various hydrological and climatological applications due to their relatively high spatial and temporal resolutions. At present, the Collection 5 (C5) suite providing snow cover area (SCA) and fractional snow cover (FSC) data, and the Collection 6 (C6)
40   suite providing normalized difference snow index (NDSI) data are the most appealing representatives (Riggs and Hall, 2015). Compared with the binary SCA of classification decision, NDSI is a remarkably detailed description of snow fraction, ranging from 0 to 100. In addition, C6 NDSI reflects the snow presence more accurately than C5 FSC because the algorithm of C6 has been carefully revised (Riggs et al., 2017). However, the main constraint of optical remote-sensed datasets, including MODIS C5 and C6 snow cover datasets, is cloud persistence.

45   Numerous algorithms have been proposed in the past decades to improve the spatio-temporal continuity of MODIS C5 snow cover datasets. Cloud removal algorithms can be categorized into single-source feature fusion methods and multi-source data fusion methods considering data sources. Single-source feature fusion methods fill the gaps based on homologous contextual information, relying on the spatio-temporal correlations of snow features. These methods have evolved from the classical Terra and Aqua combination (TAC; Parajka and Bloschl, 2008), multi-day combination (MDC; Gafurov and Bardossy,
50   2009), and snow-line method (SNOWL; Parajka et al., 2010) to complex spatio-temporal union methods. For example, Gafurov et al. (2015) proposed a four-step method to generate cloud-free MODIS SCA maps, successively combining TAC, neighborhood filtering, MDC, and classification tree. Dariane et al. (2017) suggested the aggregation of TAC, MDC, SNOWL, and neighborhood filtering with elevation constraints to fill the cloud-covered gaps. Li et al. (2017) developed an adaptive spatio-temporal weighted method to reclassify the cloudy pixels. These methods for binary SCA mapping have achieved
55   satisfactory cloud removal effectiveness and accuracy. Multi-source data fusion methods (Akyurek et al., 2010; Brown et al., 2010; Chen et al., 2018; Gafurov et al., 2015; Gao et al., 2011; He et al., 2017) maximize the complementarity among heterogeneous datasets from optical, microwave, and/or station measurements. This type of method is effective for filling the continuous gaps in space and time when the supplementary data are of high quality in the cloud-obscured regions (Li et al., 2019). In addition to traditional methods, learning-based methods are increasingly applied to snow cover mapping due to their
60   satisfactory capabilities for nonlinear expressiveness (Yuan et al., 2020). SCA and FSC maps can be generated by exploring the relationship between snow coverage and MODIS reflectances combined with ancillary factors, including NDSI, temperature, vegetation, and terrain parameters. As a representative of learning-based methods, artificial neural networks have

been successfully utilized to model the relationship (Dobreva and Klein, 2011; Hou and Huang, 2014; Moosavi et al., 2014; Çiftçi et al., 2017; Kuter, 2021). Such methods are relatively uncertain but promising because the accuracy substantially relies

65 on the quantity and quality of training data.

Increasing studies have moved to the MODIS C6 NDSI dataset since its release in 2016. The accuracy of this dataset was evaluated through higher resolution remote-sensed images (such as Landsat and Sentinel series) and in-situ measurements (Crawford, 2015; Zhang et al., 2019; Aalstad et al., 2020). The optimal classification thresholds for the binary SCA dataset and flexible mapping methods for the FSC dataset were designed in accordance with the characteristics of different geographic

70 regions to generate new binary SCA (Huang et al., 2018; Malmros et al., 2018; Tong et al., 2020) and FSC maps (Kuter et al., 2018; Hou et al., 2020; Zhang et al., 2021) superior to the C5 datasets. In terms of cloud removal from the NDSI dataset, several gap-filling methods with an associated concern of spatial and temporal correlations of snow presence were proposed (Jing et al., 2019; Chen et al., 2020; Li et al., 2020). However, the applicability of the aforementioned methods to NDSI mapping must be improved despite their good performance in binary SCA mapping. Among these methods, the spatio-temporal

75 feature-based methods with relatively high robustness are more effective for improving NDSI datasets (Jing et al., 2019).

Many studies on snow monitoring in China are available, and most of these studies focus on binary SCA mapping. On the regional scale, TP, which is known as the world's third pole, plays a key role in the global climate system. Nevertheless, snow cover mapping is particularly challenging over TP due to the frequent cloud cover resembling fragmented snow. A large number of studies have demonstrated that the snow cover variability over TP is extremely complex, with significant spatio-

80 temporal heterogeneity (Gao et al., 2012; Tang et al., 2013; Yu et al., 2016; Liang et al., 2017; Zhang et al., 2012). XJ (Wang et al., 2008) and NC (Che et al., 2016) located in mid-latitude areas are dominated by seasonal snow cover. Che et al. (2019) presented an integrated snow cover dataset from a distributed hydrometeorological observation network in the Heihe River Basin, which achieved a prominent demonstration of data synthesis at a watershed scale. In addition, the large-scale transient snow cover areas increase the level of challenge for generating high-quality snow cover datasets. On the national scale, Huang

85 et al. (2016) obtained the cloud-removed SCA products from December 2000 to October 2014 using a multi-source data fusion method. However, continuous NDSI datasets with detailed information on snow cover extent are still scarce.

A daily spatio-temporal continuous MODIS C6 NDSI dataset with a spatial resolution of 500 m for China (Fig. 1) from 2001 to 2020 is generated for the first time. A Spatio-Temporal Adaptive fusion method with erroR correction (STAR) improved from our previous work (Jing et al., 2019) is utilized to eliminate cloud obscuration. The long-term detailed snow

90 cover extent dataset will facilitate snow-related scientific studies and practical applications. The rest of this paper is arranged as follows. Section 2 describes the input data and the proposed cloud removal method. Section 3 presents the validation experiments, with a subsequent analytical application. Section 4 introduces data availability, and Section 5 provides the conclusions with future perspectives.

2 Data and Methods

2.1 Input data

95

MODIS sensors onboard Terra and Aqua satellites provide the global snow cover datasets. The daily snow cover datasets of C6 (MOD10A1 and MYD10A1 from Terra and Aqua, respectively), which are available through the website of the National Aeronautics and Space Administration (NASA, https://search.earthdata.nasa.gov/), were used in this study. As shown in Fig. 1, the NDSI of 19 tiles covering China (excluding sea area) from 1 August 2000 to 31 July 2020, was acquired to generate snow cover maps. The 90 m digital elevation model (DEM) dataset of Shuttle Radar Topographic Mission (SRTM) was obtained from the United States Geological Survey (USGS). In addition, the snow depth data respectively derived from 49 and 92 meteorological stations in XJ and TP (Tibet Meteorological Bureau and National Meteorological Information, 2018) were used for site validation. Since the snow depth data can only assess the classification performance of MODIS NDSI retrievals, the NDSI maps derived from Landsat OLI images were utilized for comprehensive validation.

100

105
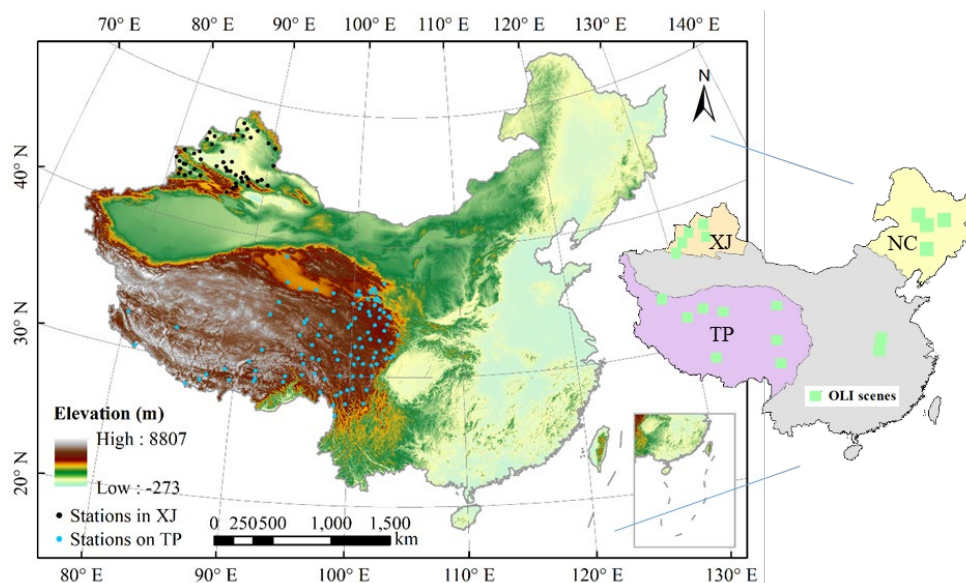
Figure 1. Topographic relief of China, meteorological stations in XJ and TP, and Landsat OLI scenes used for validation.

2.2 Algorithm description

MODIS NDSI datasets are unable to represent the daily conditions of snow accumulation and ablation accurately because the optical remote-sensed images are subject to severe cloud pollution. Therefore, a Spatio-Temporal Adaptive fusion method with erroR correction (STAR), which is derived from our two-stage spatio-temporal fusion method (Jing et al., 2019), is presented to produce a spatio-temporal continuous snow collection. As shown in Fig. 2, the generation procedure comprises the pre-process TAC and the key-process STAR. Then, a quality assessment (QA) approach is presented to provide a data reliability

110

profile for users. On this basis, post-processing is used to further improve the data quality in individual abnormal areas.

115
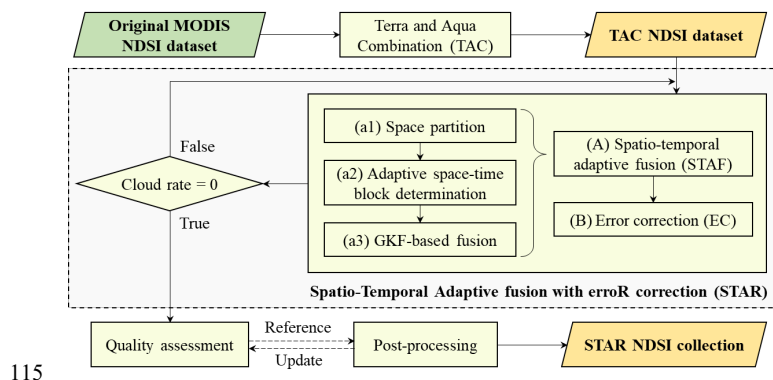
Figure 2. Schematic of the generation procedure of the STAR NDSI collection.

2.2.1 Terra and Aqua combination (TAC)

TAC blends the same-day snow maps deriving from MODIS sensors aboard on Terra and Aqua satellites. Its cornerstone is the unlikely significant changes of the snow pattern within the data-acquired time interval (approximately 3 h). The improved

120 Aqua MODIS C6 NDSI dataset significantly enhances the effectiveness of TAC due to the successful restoration of the absent Aqua MODIS band 6 data by the quantitative image restoration method (Gladkova et al., 2012). TAC can efficiently decrease the cloud fraction by 5%–20% with negligible precision sacrifice (Li et al., 2019). Thus, this method is introduced as a pre-processing to reduce cloud coverage preliminarily. Its priority scheme is determined as high value > low value > cloud. Particularly, the snow in low altitude and low latitude areas during summer is reversed to no snow to alleviate commission

125 errors inherited from the original data.

2.2.2 Spatio-Temporal Adaptive fusion with erroR correction (STAR)

Many regions with persistent clouds are out of the scope of TAC. To this end, an advanced STAR method, which comprehensively utilizes spatio-temporal contextual information, is proposed to remove the clouds thoroughly. As shown in Fig. 3, the method performs in two passes: spatio-temporal adaptive fusion (STAF) and error correction (EC).

130 The first pass involves the generation of new NDSI maps by adaptively merging the spatio-temporal contextual information, including space partition, adaptive space-time block determination, and Gaussian Kernel function (GKF)-based fusion. The research area is first segmented into dozens of partitions considering the spatial heterogeneity of snow patterns. Thus, the subsequent processes can be performed on a partition basis. Moreover, the optimal query partitions (Q) to each target partition (T) are determined by a comprehensive consideration of temporal distance (t), regional correlation (r), and cloud-free

135 fraction (f) concerning the temporal complexity of snow variations. The following optimal parameters are derived from the extensive experiments.

$$\begin{cases} \text{Scheme 1: } r > 0.7, & \text{if } f^{C\&T} > 0.3 \\ \text{Scheme 2: } max(r^1 + f^C), & \text{others} \end{cases}.$$ (1)

The regional correlation between the candidate partition (C) within an eight-day window and the target partition is considered representative if the fraction of the intersecting cloud-free areas ($f^{C\&T}$) is higher than 0.3. The candidate partition is then

140 determined as a query partition according to Scheme 1 when the regional correlation is larger than 0.7. Otherwise, Scheme 2 is activated. Two query partitions with short distance and high cloud-free fraction are identified within the preceding eight days and the backward eight days, respectively. Subsequently, the 3 × 3 neighborhoods for each pixel of the target partition in all the associated query partitions are determined as the space-time reference block. Last, each pixel is reassigned a fused value from the related space-time block, as expressed in Eq. (2):

145 $NDSI_i^F = \sum_{t=1}^{M} \sum_{s=1}^{N} w_{(i,st)} \times NDSI_{(i,st)}^Q,$

where $W_{(i,st)} = r_t^2 \times exp\left(\frac{-\left(\left(\varepsilon \Delta s_{(i,s)}\right)^2 + \Delta t_{(i,t)}^2\right)}{2\sigma^2}\right),$ (2)

where $NDSI_i^F$ denotes the fused NDSI of Pixel i in the target partition. $NDSI_{(i,st)}^Q$ is the pre-processed NDSI in associated query partitions. M is the number of query partitions, each of which contains N reference pixels. In addition, the weight $W_{(i,st)}$ is assigned by a two-dimensional GKF involving the spatial distance ($\Delta s_{(i,s)}$) and the temporal distance ($\Delta t_{(i,t)}$), which is

150 then normalized to $w_{(i,st)}$. σ is the standard deviation of GKF. ε characterizes the dimensional difference, which is equal to σ_t/σ_s with an expression of each single-dimensional GKF. r_t represents the regional correlation between the query and target partitions if Scheme 1 works; otherwise, it is ignored (i.e., $r_t = 1$). The constant term ($\varepsilon/2\pi\sigma^2$) of GKF is ignored due to the normalization process. The important parameters in STAF are listed in Table 1.

155 **Table 1. Description and default values of STAF parameters.**

Parameter	Description	Value
W_T	Temporal window for query partition	±8 day
W_N	Neighboring window for reference pixel	3 × 3
r	Minimum regional correlation for query partition	0.7
σ	Standard deviation in the GKF	0.5
ε	Dimensional difference coefficient (σ_t/σ_s) in the GKF	25/9

The second pass corrects the fused NDSI maps considering the spatial correlation within a partition. Specifically, the residual errors of the intersecting cloud-free areas of the pre-processed and fused NDSI maps (refer to as $NDSI^P$ and $NDSI^F$) are diffused to other cloud-free areas of the fused NDSI maps using the triangulation-based natural neighbor interpolation

160 (Sibson et al., 1981). Then, the high-quality NDSI maps ($NDSI^H$) can be generated by removing all errors from the fused NDSI maps. The process is formulated as follows:

$$\begin{cases} E_R = NDSI_R^F - NDSI_R^P \\ E_{T(i)} = \sum_{n=1}^{N'} \phi_{(i,n)} E_{R(i,n)}, \\ NDSI_T^H = NDSI_T^F - E_T \end{cases}$$ (3)

where R indicates the reference area which is the boundary of the intersecting cloud-free areas. T indicates the target area. The

165 dynamic weights in the error diffusion from E_R to E_T are based on the Voronoi diagrams. As expressed in Fig. 3 (b-left), the original Voronoi cells (bounded by red and gray solid lines) of the reference pixels (gray dots) intersect with the new Voronoi cells (bounded by blue and gray solid lines) of the reference and target pixels. Taking the target pixel T_1 with the reference pixel R_1 as an example, the weight is assigned as the ratio of the area of the intersecting Voronoi cell (A_{dabch}) to that of the new Voronoi cell (A_{defgh}).

$$\phi_{(1,1)} = \frac{A_{dabch}}{A_{defgh}}. \tag{4}$$

170 After all the partitions are processed in sequence, the next iteration of STAR begins until the clouds are completely removed.
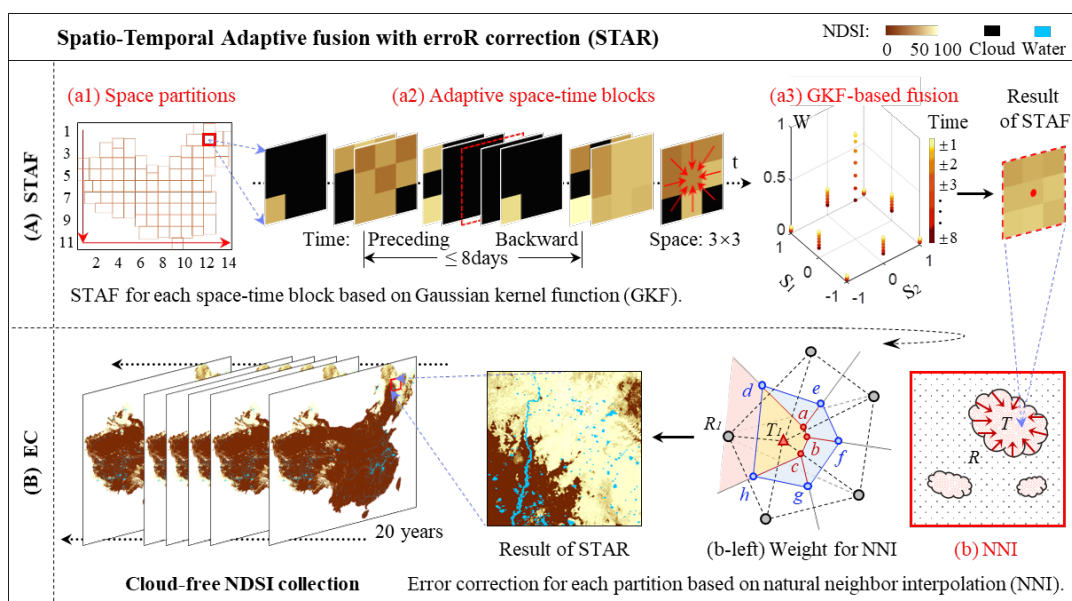
Figure 3. Detailed flowchart of the Spatio-Temporal Adaptive fusion with erroR correction (STAR).

2.2.3 Quality assessment (QA) approach

175 A revised QA approach for the gap-filled NDSI collection is proposed on the basis of the quality estimate of MODIS NDSI datasets (Riggs and Hall, 2015), and an example is presented in Fig. A1 (Appendix A). Users can examine the basic quality of the gap-filled NDSI collection considering cloud coverage and spatio-temporal consistency of the raw NDSI dataset by retrieving the bit flags from the integer stored in QA maps. The specific attributes are listed in Table 2.

The snow detection reversal of the pre-processed value in TAC is tracked in Bit 2, the post-processing (Sect. 2.2.4) is

180 tracked in Bit 3, and the number of iterations primarily related to cloud coverage is indicated by Bit 4. If the range of reference values is larger than 30, then Bit 5 flag is set; if the difference of pre-processed and fused values is larger than 20, then Bit 6 flag is set. Bit 7 reflects the cloud coverage of the space-time block. Furthermore, the combination of Bits 0 and 1 is a qualitative

estimate of the cloud-removed NDSI collection based on the number of iterations (from here on referred to as NI) and spatio-temporal consistency. The comprehensive estimate is determined as follows:

185   ─ if NI = 5 and Bit 5 or 6 is set to 1, then it is assigned "poor";

─ if NI = 4 and Bit 5 or 6 is set to 1, then it is assigned "OK";

─ if NI = 3 and Bit 5 or 6 is set to 1, then it is assigned "good";

─ otherwise, it is assigned "best".

The QA maps are recommended for in-depth application of the cloud-removed NDSI collection.

190

Table 2. Bit flags indicating the retrieval conditions according to the raw NDSI dataset.

Bit	Description	Bit Combination	Quality
0–1	Comprehensive estimate	00	Best
		01	Good
		10	OK
		11	Poor
2	Pre-processing	0	None
		1	Snow detection reversed
3	Post-processing	0	None
		1	Post-processed
4	Number of iterations	0	No more than 3
		1	More than 3
5	Consistency between reference values	0	Consistent
		1	Inconsistent
6	Consistency between pre-processed and fused values	0	Consistent
		1	Inconsistent
7	Cloud coverage of the space-time block	0	Low [0,60%)
		1	High [60%,1]

2.2.4 Post-processing

For areas with extremely rapid and fluctuating snow variation, the temporal contextual references are likely to introduce

195   incorrect information and magnify errors in the iterative process. Post-processing is used in this study to reduce the "disorder" phenomenon referring to QA maps. Firstly, the NDSI map with the most consistent snow pattern in adjacent time is artificially identified as a reference. Subsequently, the aforementioned EC is applied to improve the spatial consistency between the post-processing and original areas. Finally, the QA maps are updated.

2.3 Validation of the NDSI collection

200   The gap-filled NDSI collection is evaluated with the in-situ snow depth observations and Landsat NDSI maps considering

classification and numerical accuracies according to the current mature verification methods. As shown in Table 3, the classification metrics based on the confusion matrix include overall accuracy (OA), commission error (CE), and omission error (OE) (Klein and Barnett, 2003). Moreover, three general metrics are introduced to measure numerical accuracy: correlation coefficient (CC), absolute error (AE), and root-mean-square error (RMSE).

205

Table 3. Confusion matrix and validation metrics.

	MODIS NDSI datasets	
In-situ observations	NDSI > 0	NDSI = 0
Snow depth > 0 cm	SS	SN
Snow depth = 0 cm	NS	NN

$$OA = \frac{SS + NN}{SS + SN + NS + NN} \quad CE = \frac{NS}{NS + NN} \quad OE = \frac{SN}{SN + SS}$$

3 Results

As mentioned above, the generation procedure of continuous snow collection includes the pre-process TAC and the key-

210 process STAR. The remainder clouds of 30.62% in the entire collection after TAC are completely removed by STAR. Based on in-situ snow depth measurements and Landsat NDSI maps, this section presents the evaluation results of the STAR NDSI collection compared with the TAC NDSI dataset, followed by an exemplary application.

3.1 Validation against in-situ snow depth measurements

As described above, the in-situ snow depth data in XJ from 1 August 2000 to 31 August 2007 and on TP from 1 August 2000

215 to 31 December 2013, were used as the ground truth to evaluate the classification accuracy of TAC NDSI and STAR NDSI datasets. The nearest pixel was matched with each meteorological station, with a total of about 600000 data pairs. Snow-clad pixels in both NDSI datasets range from 10 to 100, whereas snow-free pixels are 0; thus, the classification threshold is set as 10 (Zhang et al., 2019). The discriminant threshold for in-situ snow depth is set as 0 or 1 cm. In addition, the cloud-covered areas in the TAC NDSI dataset are considered to be snow-free.

220 Table 4 demonstrates that the STAR NDSI collection preeminently captures the snow dynamics in XJ referring to the in-situ measurements, with an OA reaching 0.95. However, the TAC NDSI dataset is insufficient to accurately describe the snow cover variability. Although CEs perform well regardless of the snow depth threshold, OEs of the TAC NDSI collection are extremely high, indicating that many cloud-covered areas are dominated by snow. The STAR NDSI collection completely removes clouds and accurately presents snow distribution, with an OE decreased from ~60% to ~6%. The generation procedure

225 in XJ has two strengths. First, the satellite-borne sensors can accurately capture the snow events on the ground due to the generally thick snow averaging approximately 20 cm. Second, the gap-filling approach with comprehensive consideration of

spatial and temporal correlation has outstanding reliability due to the significant periodicity of snow variation. It can be inferred that the NDSI datasets in NC have high accuracy because of the similar snow conditions, despite the lack of in-situ data in this region.

230   By contrast, despite the satisfactory performance of OAs and CEs, the OEs of two NDSI datasets over TP are as remarkably high as 72% and 39% even at the snow depth threshold of 1 cm (Table 5). This finding indicates the omission of a large number of snow-covered pixels. The specific reasons are as follows. First, the original MODIS NDSI maps frequently underestimate the snow presence throughout the snow period because discriminating the shallow snow pixels with an averaged snow depth of approximately 4 cm over TP is challenging. Second, the credibility of the spatio-temporal contextual information

235   is relatively low because the snow rapidly and irregularly varies due to the extremely complex topographic and climatic conditions, leading to a further decrease in the accuracy of the gap-filled results. Last, the meteorological stations over TP are unevenly distributed and are mostly located in low- and medium-altitude/latitude areas dominated by transient snow. Consequently, the evaluation results slightly exaggerate the real OEs.

Overall, the STAR NDSI collection is capable of snow status estimation, eliminating cloud contamination in the TAC

240   NDSI dataset. However, the accuracy of the STAR NDSI collection has a significant regional heterogeneity. On the one hand, the accuracy over TP is lower than that of XJ and NC, which is consistent with the characteristic of the original MODIS NDSI maps. On the other hand, the permanent and periodic snow regime regions reconstructed by STAR have prominently high accuracy, while the transient snow-covered regions are easily omitted. Fortunately, the monitoring of permanent and periodic snow plays a key role in most snow-related investigations.

245

Table 4. Classification statistics based on in XJ.

Indicators	Snow depth > 0 cm (Snow fraction = 30%)		Snow depth > 1 cm (Snow fraction = 28%)	
	TAC	STAR	TAC	STAR
OA	0.81	0.95	0.82	0.95
CE	0.02	0.04	0.02	0.05
OE	0.60	0.06	0.58	0.05

Table 5. Classification statistics over TP.

Indicators	Snow depth > 0 cm (Snow fraction = 5%)		Snow depth > 1 cm (Snow fraction = 3%)	
	TAC	STAR	TAC	STAR
OA	0.94	0.95	0.96	0.96
CE	0.01	0.03	0.02	0.03
OE	0.78	0.52	0.72	0.39

3.2 Validation based on Landsat NDSI maps

Only the classification accuracy can be evaluated by in-situ measurements due to the significant difference in the nature of the snow depth and NDSI data. Therefore, Landsat images with finer spatial resolution were commonly adopted for the numerical

250   evaluation of NDSI datasets (Crawford, 2015). NDSI values for the Landsat 8 dataset were calculated as follows: (*Band3 - Band6*) / (*Band3 + Band6*). Subsequently, the average of the 17 × 17 neighborhoods closest to the center of the MODIS NDSI pixel in the Landsat NDSI map was considered to be the reference of this MODIS NDSI pixel to match the

spatial resolution of Landsat with that of MODIS. Specifically, the cloud-contaminated pixels marked by the quality band in Landsat images were excluded, and the reference areas with cloud coverage larger than 30% were discarded. A total of 19

255 Landsat NDSI maps with different snow coverages from January to April in 2018, which are distributed in NC (4 scenes), Central China region (CCR; 2 scenes), TP (8 scenes), and XJ (5 scenes), were exploited as evaluation references for this validation experiment. Two evaluations include a comparison of TAC and STAR NDSI datasets and a comparison of clear-sky and cloud-cover areas are described in detail below.

As the average cloud cover is as high as 40.7%, the TAC NDSI dataset has a low correlation with Landsat NDSI maps,

260 with an average CC of 0.46 (Table 6). By contrast, the STAR NDSI collection is a spatio-temporal continuous dataset. The snow dynamics presented by the STAR NDSI dataset are highly consistent with Landsat NDSI maps, with an average CC of approximately 0.84. The average RMSE of the STAR NDSI dataset is decreased by 9.06 compared with the TAC NDSI dataset. NDSI values for snow pixels in the STAR NDSI dataset are generally higher than that of Landsat NDSI maps. In terms of snow coverage, the STAR NDSI dataset notably improves the detection of snow events, with an average absolute SRD

265 decreased from 33.0% to 1.9% (SRD indicates the difference of snow rate between MODIS and Landsat NDSI datasets). Consequently, the STAR NDSI collection is a more promising snow cover product than the TAC NDSI dataset, contributing to related hydrological and meteorological studies.

Table 6. Performance statistics for two MODIS NDSI datasets against Landsat NDSI maps.

Region_Date	Cloud coverage (%)	CC		RMSE		AE		SRD (%)	
		STAR	TAC	STAR	TAC	STAR	TAC	STAR	TAC
NC1_20180225	61.4	0.87	0.49	17.10	25.64	15.07	-11.59	1.0	-60.1
NC2_20180311	43.6	0.83	0.69	13.87	26.75	12.14	-9.36	-1.7	-43.1
NC3_20180311	34.6	0.86	0.19	8.79	18.61	0.15	-10.26	-2.8	-34.2
NC4_20180318	16.3	0.98	0.73	10.25	21.50	5.42	-3.33	-1.1	-16.6
CCR1_20180203	14.9	0.95	0.20	5.04	11.53	1.54	-3.56	2.8	-11.4
CCR2_20180203	95.0	0.73	-0.07	8.43	14.26	0.10	-9.07	-5.4	-47.8
TP1_20180322	36.3	0.83	0.39	10.70	18.03	0.77	-5.30	1.3	-13.8
TP2_20180225	22.4	0.82	0.54	15.27	25.50	-0.30	-9.66	-9.1	-27.8
TP3_20180320	15.3	0.74	0.29	7.91	11.40	-1.49	-2.89	-3.5	-6.7
TP4_20180401	29.5	0.79	0.47	16.64	30.94	-3.71	-16.86	-8.3	-31.6
TP5_20180307	42.5	0.92	0.47	13.80	30.00	7.67	-11.76	1.0	-36.0
TP6_20180305	64.9	0.78	0.17	14.53	42.26	4.67	-32.30	-2.9	-66.1
TP7_20180107	60.8	0.80	0.44	18.08	28.13	6.04	-15.95	-12.57	-60.00
TP8_20180128	34.6	0.82	0.49	10.65	11.98	2.68	0.67	4.3	1.1
XJ1_20180105	52.2	0.86	0.79	22.81	27.53	22.18	-4.00	0.1	-52.2
XJ2_20180213	23.4	0.92	0.64	20.81	23.55	18.29	7.13	7.2	-14.8
XJ3_20180220	56.0	0.86	0.56	18.78	26.35	16.06	-9.87	1.9	-51.2
XJ4_20180103	23.5	0.74	0.70	28.86	28.94	26.66	15.70	-0.2	-21.8
XJ5_20180220	46.1	0.92	0.55	11.99	23.55	2.28	-10.44	-8.0	-32.7
Average	40.7	0.84	0.46	14.44	23.50	7.17	-7.51	-1.9	-33.0

270   In addition to the comparison between STAR NDSI and TAC NDSI datasets, an evaluation in clear-sky areas and cloud-cover areas was performed based on Landsat NDSI maps, to highlight the accuracy of the recovered pixels in the STAR NDSI collection. As described above, clear-sky areas and cloud-cover areas account for 59.3% and 40.7%, respectively. Table 7 indicates that the snow distribution of recovered areas in the STAR NDSI collection is relatively consistent with that of Landsat NDSI maps. Although the average CC decreases from 0.85 to 0.73 and the average RMSE increases from 13.48 to 16.30

275   compared with clear-sky areas, the accuracy of recovered areas is satisfactory. Since many recovered areas inherit errors from clear-sky areas because the cloud removal procedure completely relies on the original dataset, a slight decrease in accuracy is reasonable. In addition, the average AEs of clear-sky and recovered areas are 7.81 and 6.83, respectively, revealing the systematic overestimation of NDSI values in snow areas (Landsat NDSI values are generally low). Except for a few areas, the snow conditions in most cloud-cover areas are well recovered, with an average SRD of -5.0%. This finding highlights that the

280   STAR NDSI collection can completely remove clouds with a satisfactory accuracy.

Table 7. Performance statistics for the STAR NDSI collection against Landsat NDSI maps in clear-sky and cloud-cover areas according to the TAC dataset. Note: Red and blue bold values respectively indicate an improvement and degradation of cloud-cover areas compared with clear-sky areas (corresponding to four groups in Fig. 4).

Region_Date	CC		RMSE		AE		SRD (%)	
	Clear-sky	Cloud-cover	Clear-sky	Cloud-cover	Clear-sky	Cloud-cover	Clear-sky	Cloud-cover
NC1_20180225	0.95	0.76	16.89	17.23	15.23	14.97	2.91	-0.2
NC2_20180311	0.89	0.71	12.27	15.71	11.78	12.62	-0.10	-3.7
NC3_20180311	**0.92**	**0.42**	2.31	14.60	-0.09	0.61	-1.02	-6.1
NC4_20180318	0.98	0.86	10.29	14.75	4.88	11.30	-1.23	-0.2
CCR1_20180203	0.83	0.68	3.37	10.29	0.68	6.50	3.48	-0.9
CCR2_20180203	**0.55**	**0.74**	10.93	8.28	6.80	-0.25	32.63	-7.4
TP1_20180322	0.75	0.87	10.22	11.49	0.44	1.35	0.11	3.4
TP2_20180225	**0.86**	**0.64**	13.50	20.24	0.89	-4.40	-7.49	-14.8
TP3_20180320	0.73	0.69	3.74	18.19	-0.40	-7.52	-1.07	-16.9
TP4_20180401	0.79	0.78	16.56	17.08	-4.35	-2.17	-8.14	-8.3
TP5_20180307	0.94	0.88	13.82	13.86	8.01	7.16	1.68	0.1
TP6_20180305	0.79	0.76	15.03	14.26	1.75	6.24	-4.79	-1.9
TP7_20180107	0.98	0.63	15.17	19.74	10.28	3.27	-1.00	-20.0
TP8_20180128	0.75	0.89	11.13	9.92	3.27	1.67	7.62	-1.7
XJ1_20180105	0.89	0.62	24.47	21.17	24.29	20.25	0.00	0.1
XJ2_20180213	0.95	0.74	20.47	21.88	18.27	18.37	9.00	1.5
XJ3_20180220	0.93	0.75	17.45	19.77	15.37	16.60	4.02	0.2
XJ4_20180103	**0.64**	**0.58**	29.54	26.53	28.09	22.00	0.61	-2.9
XJ5_20180220	0.97	0.86	8.92	14.81	3.26	1.13	-1.31	-15.7
Average	0.85	0.73	13.48	16.30	7.81	6.83	1.89	-5.0

285
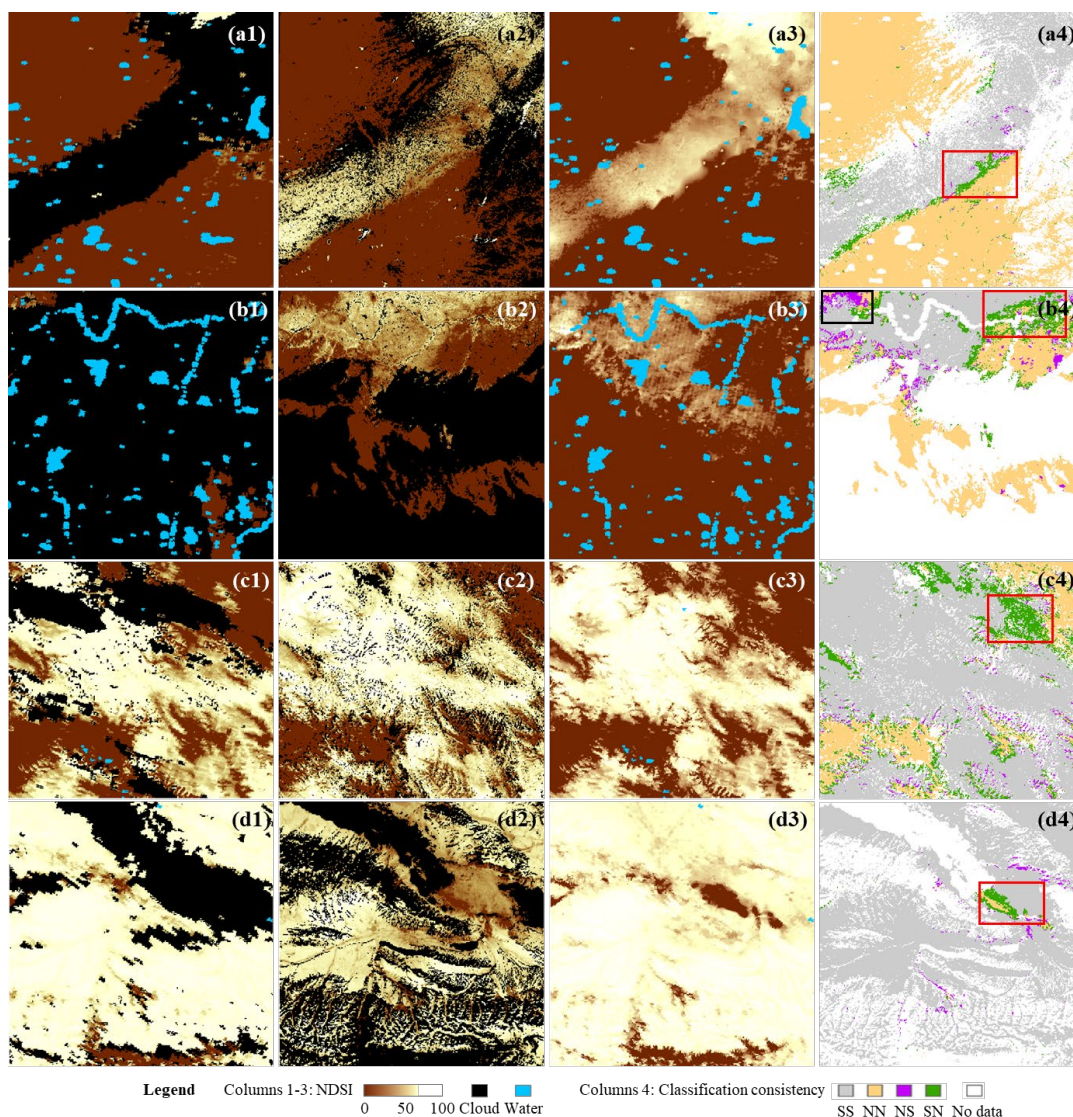
Figure 4. Comparison of TAC NDSI (column 1), Landsat NDSI (column 2), and STAR NDSI (column 3) products and classification consistency (column 4) corresponding to NC3_20180311, CCR2_20180203, TP2_20180225, and XJ4_20180103 (groups *a* to *d*).

For in-depth verification analysis, Figure 4 shows the visual effects in four regions corresponding to four highlighted groups in Table 7. The accuracy of clear-sky areas in NC is prominently high with a CC of 0.92, while recovered areas notably reduces the performance with a CC of 0.42. However, Figure 4a shows that clear-sky areas in the TAC NDSI dataset cannot reflect the snow events, whereas the STAR NDSI collection effectively retrieves these events. Inevitably, the snow edges are slightly inaccurate and blurry due to insufficient reference information. For group (b), the original accuracy of the NDSI dataset in CCR is relatively low, with high cloud coverage and false acceptance rate, while the STAR NDSI collection presents a snow pattern consistent with Landsat NDSI. Nevertheless, CCR is a transient snow area with relatively low altitudes and latitudes. Therefore, the gap-filled result has visible uncertainty, in which commission (black box) and omission (red box) frequently

occur. As mentioned above, MODIS NDSI datasets generally perform poorly over TP. However, Figure 4c demonstrates that TAC NDSI and STAR NDSI collections can accurately capture snow events despite a few omissions (red box). Similar to the NC region, the CCs provide a positive indication of overall performance in XJ. As shown in Fig. 4d, even the *XJ4_20180103* scene with a remarkably low CC of 0.58 can effectively reflect the snow pattern. In addition, the NDSI dataset retrieved by

300   STAR inevitably has a few extremely abnormal areas during 20 years due to the vast territory of China; an example is presented in Fig. A2 (Appendix A). These areas have severe cloud contamination and irregular snow dynamics, contributing to the challenges in reconstruction and evaluation. Therefore, these areas are corrected by post-processing as described in Sect. 2.2.4.

Overall, the numerical evaluation based on fine-resolution remote-sensed images indicates that the STAR NDSI collection eliminates cloud contamination and preeminently improves the overall performance of the TAC NDSI dataset. Although

305   recovered areas have slightly lower accuracy than clear-sky areas, the effectiveness of cloud removal is satisfactory. Therefore, the STAR NDSI collection has considerable application potential.

3.3 Application of the STAR NDSI collection

In addition to quality evaluation, the exemplary analysis also contributes to understanding the collection potential for hydrological and climatic applications. From a spatial perspective, the sequence shown in Fig. 5 indicates that the snow

310   coverage first increases and then decreases in NC and XJ regions but considerably fluctuates on TP. Figure 6 reveals that all subregions present a single-wave depletion curve in early 2020. Compared with the previous sequence, the snow cover variation on TP in this sequence has significantly enhanced regularity.
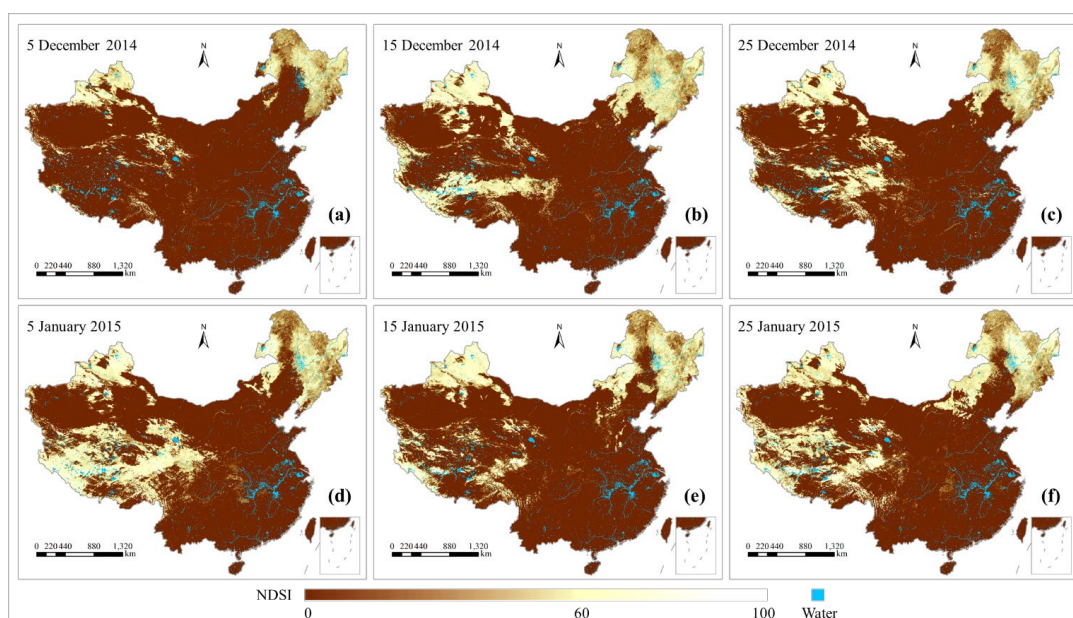
Figure 5. Sequence of the STAR NDSI collection from 5 December 2014 to 25 January 2015.
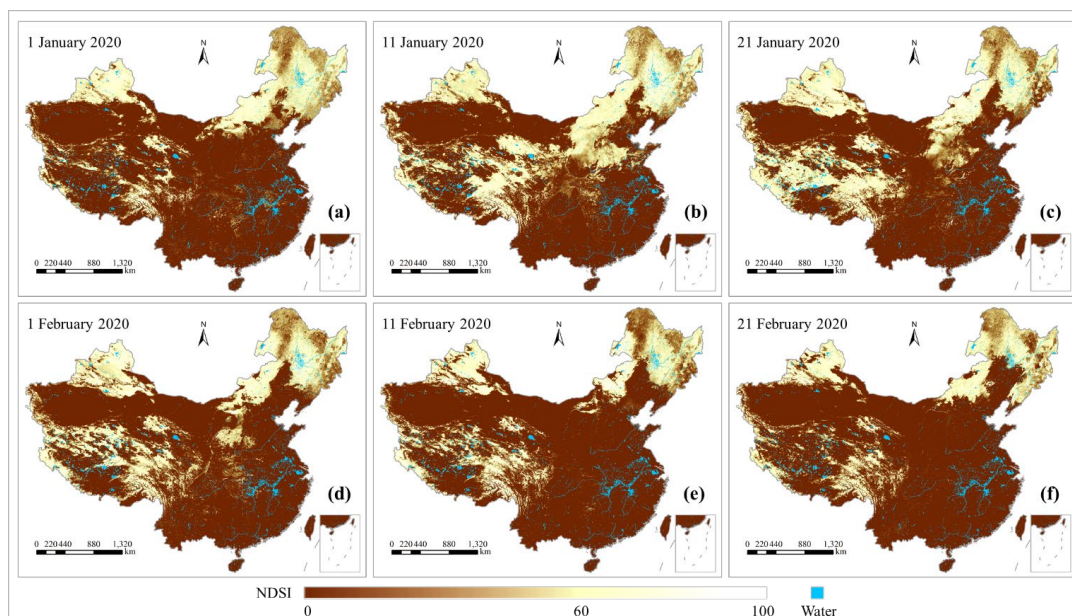
Figure 6. Sequence of the STAR NDSI collection from 1 January 2020 to 21 February 2020.

Figure 7 shows the daily average snow fraction in the three main subregions in China and the entire situation considering temporal analysis. In terms of intra-annual variability, the snow dynamics periodically evolve in XJ and NC but substantially fluctuates on TP. XJ and NC have similar snow depletion curves, demonstrating rapid accumulation and ablation in November and March, respectively. TP has a relatively long snow period, with an average snow fraction varying from 20% to 40% from October to next May. Consequently, China is dominated by periodic snow. As for inter-annual variability, among the three major snow areas, the snow fraction in NC remarkably fluctuates with a standard deviation of 5.3%. The snow coverage on TP presented a slight decreasing trend from 2005 to 2017 but increased significantly in the past two years. In particular, rather than a significant rise in maximum snow coverage, the increase can be observed throughout the snow period with a slight reduction in intra-annual volatility. This finding implies that the regional climatic conditions tend to stabilize slightly. In addition, no significant trend has been detected in snow dynamics in China during the 20 years. Nevertheless, the significant fluctuation of maximum snow coverage in China indicates the presence of non-negligible large-scale transient snow cover areas. For example, Figure A3 (Appendix A) shows the extreme snow event in southern China caused by the La Niña phenomenon, which resulted in heavy casualties and economic losses in the hydrological year 2007–2008. Overall, the STAR NDSI collection can accurately reflect the snow cover dynamics in China and potentially be applied for hydrological and meteorological modeling.
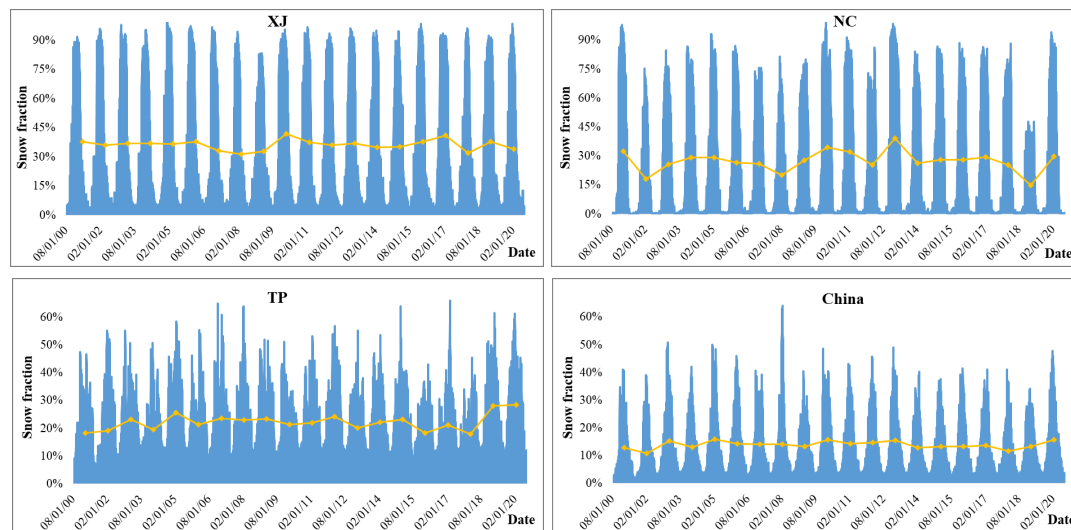
Figure 7. Daily average snow fraction of XJ, NC, TP, and China.

4 Data availability

The improved cloud-free MODIS NDSI collection (STAR NDSI collection) for China from 1 August 2000 to 31 July 2020, including STAR NDSI and STAR QA data, is available for download at https://doi.org/10.5281/zenodo.5644386 (Jing et al., 2021). The dataset is provided using a WGS 84 / UTM zone 48N projection, with a tag image file format (TIFF). Users can discuss and respond to issues that arise during the use of this dataset. New versions can be released in consideration of user comments.

5 Conclusions

The STAR NDSI collection is derived from the MODIS NDSI dataset using an optimized STAR from our last research (Jing et al., 2019). The evaluation tests indicate that the STAR NDSI collection is highly consistent with the in-situ snow depth measurements and higher resolution NDSI maps. The STAR NDSI collection generally has the following strengths. (1) This collection has reached a continuous 20-year period, which is the minimum period of a dataset for long-term hydrological and climatic processes analysis. (2) The cloud-free collection significantly improves the snow dynamics estimation compared with the TAC NDSI dataset, with a satisfactory accuracy in original cloud-cover areas. (3) The collection provides a detailed snow cover dataset in China for the first time, accurately reflecting the snow conditions of the following three major snow areas: XJ, NC, and TP. The collection is available at: https://doi.org/10.5281/zenodo.5644386 (Jing et al., 2021).

As discussed above, the STAR NDSI collection still has some deficiencies. A future release should consider several issues: (1) the original accuracy of the MODIS NDSI dataset reduced by factors such as complex climatic conditions and dense forest coverage; (2) the reconstruction accuracy of snow edges affected by mixed pixels and high cloud coverage; (3) the

350 reconstruction accuracy of transient snow areas due to the inadequate spatio-temporal contextual information; and (4) the lack

of evaluation based on in-situ snow depth measurements in NC due to the limited access to climate station data.

Despite the aforementioned deficiencies, since snow is a pivotal driver and sensitive indicator for many hydrometeorological processes, the daily 500 m STAR NDSI collection for 20 years has various potential applications: (1) achieving a deep understanding of long-term snow cover variability in China, (2) providing effective forcing data for

355 hydrological and meteorological models, and (3) supporting strategic decisions on water resources management, environmental pollution governance, and related economic development.

Author contributions. All authors designed the methodology. YJ implemented the experiments. YJ maintained and refined the STAR NDSI collection. YJ drafted the manuscript. XL and HS revised the whole manuscript. All authors provided suggestions for this manuscript.

360 **Competing interests.** The authors declare that they have no conflict of interest.

Acknowledgements. This research was supported by the National Natural Science Foundation of China (NSFC) under Grant No. 41701394. Thanks to Liupeng Lin and Menghui Jiang for their constructive suggestions.

References

Aalstad, K., Westermann, S., and Bertino, L.: Evaluating satellite retrieved fractional snow-covered area at a high-Arctic site
365   using terrestrial photography, Remote Sens. Environ., 239, 111618, https://doi.org/10.1016/j.rse.2019.111618, 2020.
Akyurek, Z., Hall, D. K., Riggs, G. A., and Sensoy, A.: Evaluating the utility of the ANSA blended snow cover product in the
        mountains of eastern Turkey, Int. J. Remote Sens., 31, 3727-3744, https://doi.org/10.1080/01431161.2010.483484, 2010.
Barnett, T. P., Adam, J. C., and Lettenmaier, D. P.: Potential impacts of a warming climate on water availability in snow-
        dominated regions, Nature, 438, 303-309, https://doi.org/10.1038/nature04141, 2005.
370   Bormann, K. J., Brown, R. D., Derksen, C., and Painter, T. H.: Estimating snow-cover trends from space, Nat. Clim. Change,
        8, 923-927, https://doi.org/10.1038/s41558-018-0318-3, 2018.
Brown, R., Derksen, C., and Wang, L. B.: A multi-data set analysis of variability and change in Arctic spring snow cover extent,
        1967-2008, Journal of Geophysical Research-Atmospheres, 115, D16111, https://doi.org/10.1029/2010jd013975, 2010.
Che, T., Dai, L. Y., Zheng, X. M., Li, X. F., and Zhao, K.: Estimation of snow depth from passive microwave brightness
375   temperature data in forest regions of northeast China, Remote Sens. Environ., 183, 334-349,
        https://doi.org/10.1016/j.rse.2016.06.005, 2016.
Che, T., Li, X., Liu, S., Li, H., Xu, Z., Tan, J., Zhang, Y., Ren, Z., Xiao, L., Deng, J., Jin, R., Ma, M., Wang, J., and Yang, X.:
        Integrated hydrometeorological, snow and frozen-ground observations in the alpine region of the Heihe River Basin, China,
        Earth Syst. Sci. Data, 11, 1483-1499, https://doi.org/10.5194/essd-11-1483-2019, 2019.
380   Chen, S., Wang, X., Guo, H., Xie, P., and Sirelkhatim, A. M.: Spatial and temporal adaptive gap-filling method producing daily
        cloud-free NDSI time series, IEEE J. Sel. Top. Appl. Earth Obs. Remote Sens., 13, 2251-2263,
        https://doi.org/10.1109/JSTARS.2020.2993037, 2020.
Chen, X. N., Long, D., Liang, S. L., He, L., Zeng, C., Hao, X. H., and Hong, Y.: Developing a composite daily snow cover
        extent record over the Tibetan Plateau from 1981 to 2016 using multisource data, Remote Sens. Environ., 215, 284-299,
385   https://doi.org/10.1016/j.rse.2018.06.021, 2018.

Çiftçi, B. B., Kuter, S., Akyürek, Z., and Weber, G. W.: Fractional snow cover mapping by artificial neural networks and support vector machines, ISPRS Annals of the Photogrammetry, Remote Sensing and Spatial Information Sciences, 4, 179-187, https://doi.org/10.5194/isprs-annals-IV-4-W4-179-2017, 2017.

Crawford, C. J.: MODIS Terra Collection 6 fractional snow cover validation in mountainous terrain during spring snowmelt
390   using Landsat TM and ETM, Hydrol. Processes, 29, 128-138, https://doi.org/10.1002/hyp.10134, 2015.

Dariane, A. B., Khoramian, A., and Santi, E.: Investigating spatiotemporal snow cover variability via cloud-free MODIS snow cover product in Central Alborz Region, Remote Sens. Environ., 202, 152-165, https://doi.org/10.1016/j.rse.2017.05.042, 2017.

Dobreva, I. D., and Klein, A. G.: Fractional snow cover mapping through artificial neural network analysis of MODIS surface
395   reflectance, Remote Sens. Environ., 115, 3355-3366, https://doi.org/10.1016/j.rse.2011.07.018, 2011.

Gafurov, A., and Bardossy, A.: Cloud removal methodology from MODIS snow cover product, Hydrol. Earth Syst. Sci., 13, 1361-1373, https://doi.org/10.5194/hess-13-1361-2009, 2009.

Gafurov, A., Vorogushyn, S., Farinotti, D., Duethmann, D., Merkushkin, A., and Merz, B.: Snow-cover reconstruction methodology for mountainous regions based on historic in situ observations and recent remote sensing data, The
400   Cryosphere, 9, 451-463, https://doi.org/10.5194/tc-9-451-2015, 2015.

Gao, J., Williams, M. W., Fu, X. D., Wang, G. Q., and Gong, T. L.: Spatiotemporal distribution of snow in eastern Tibet and the response to climate change, Remote Sens. Environ., 121, 1-9, https://doi.org/10.1016/j.rse.2012.01.006, 2012.

Gao, Y., Xie, H. J., and Yao, T. D.: Developing Snow Cover Parameters Maps from MODIS, AMSR-E, and Blended Snow Products, Photogramm. Eng. Remote Sens., 77, 351-361, https://doi.org/10.14358/pers.77.4.351, 2011.

405   Gladkova, I., Grossberg, M., Bonev, G., Romanov, P., and Shahriar, F.: Increasing the accuracy of MODIS/Aqua snow product using quantitative image restoration technique, IEEE Geosci. Remote Sens. Lett., 9, 740-743, https://doi.org/10.1109/LGRS.2011.2180505, 2012.

Hall, D. K., Riggs, G. A., and Salomonson, V. V.: Development of methods for mapping global snow cover using Moderate Resolution Imaging Spectroradiometer data, Remote Sens. Environ., 54, 127-140, https://doi.org/10.1016/0034-
410   4257(95)00137-P, 1995.

He, G. J., Feng, X. Z., Xiao, P. F., Xia, Z. H., Wang, Z., Chen, H., Li, H., and Guo, J. J.: Dry and Wet Snow Cover Mapping in Mountain Areas Using SAR and Optical Remote Sensing Data, IEEE J. Sel. Top. Appl. Earth Obs. Remote Sens., 10, 2575-2588, https://doi.org/10.1109/jstars.2017.2673409, 2017.

Hou, J., and Huang, C.: Improving mountainous snow cover fraction mapping via artificial neural networks combined with
415   MODIS and ancillary topographic data, IEEE Trans. Geosci. Remote Sens., 52, 5601-5611, https://doi.org/10.1109/TGRS.2013.2290996, 2014.

Hou, J., Huang, C., Zhang, Y., and Guo, J.: On the Value of Available MODIS and Landsat8 OLI Image Pairs for MODIS Fractional Snow Cover Mapping Based on an Artificial Neural Network, IEEE Trans. Geosci. Remote Sens., 58, 4319-4334, https://doi.org/10.1109/TGRS.2019.2963075, 2020.

420   Huang, X. D., Deng, J., Ma, X. F., Wang, Y. L., Feng, Q. S., Hao, X. H., and Liang, T. G.: Spatiotemporal dynamics of snow cover based on multi-source remote sensing data in China, The Cryosphere, 10, 2453-2463, https://doi.org/10.5194/tc-10-2453-2016, 2016.

Huang, Y., Liu, H. X., Yu, B. L., We, J. P., Kang, E. L., Xu, M., Wang, S. J., Klein, A., and Chen, Y. N.: Improving MODIS snow products with a HMRF-based spatio-temporal modeling technique in the Upper Rio Grande Basin, Remote Sens.
425   Environ., 204, 568-582, https://doi.org/10.1016/j.rse.2017.10.001, 2018.

Jing, Y. H., Shen, H. F., Li, X. H., and Guan, X. B.: A Two-Stage Fusion Framework to Generate a Spatio-Temporally Continuous MODIS NDSI Product over the Tibetan Plateau, Remote Sensing, 11, 2261, https://doi.org/10.3390/rs11192261, 2019.

Jing, Y. H., Li, X. H., and Shen, H. F.: STAR NDSI collection: A cloud-free MODIS NDSI dataset (2001–2020) for China
430   (Version 01) [Data set], Zenodo, https://doi.org/10.5281/zenodo.5644386, 2021.

Klein, A. G., and Barnett, A. C.: Validation of daily MODIS snow cover maps of the Upper Rio Grande River Basin for the 2000-2001 snow year, Remote Sens. Environ., 86, 162-176, https://doi.org/10.1016/S0034-4257(03)00097-X, 2003.

Konzelmann, T., and Ohmura, A.: Radiative fluxes and their impact on the energy-balance of the Greenland ice-sheet, J. Glaciol., 41, 490-502, https://doi.org/10.3189/s0022143000034833, 1995.

435 Kuter, S., Akyurek, Z., and Weber, G. W.: Retrieval of fractional snow covered area from MODIS data by multivariate adaptive regression splines, Remote Sens. Environ., 205, 236-252, https://doi.org/10.1016/j.rse.2017.11.021, 2018.

Kuter, S.: Completing the machine learning saga in fractional snow cover estimation from MODIS Terra reflectance data: Random forests versus support vector regression, Remote Sens. Environ., 255, 112294, https://doi.org/10.1016/j.rse.2021.112294, 2021.

440 Li, M., Zhu, X., Li, N., and Pan, Y.: Gap-Filling of a MODIS normalized difference snow index product based on the similar pixel selecting algorithm: A case study on the Qinghai-Tibetan Plateau, Remote Sensing, 12, 1077, https://doi.org/10.3390/rs12071077, 2020.

Li, X. H., Fu, W. X., Shen, H. F., Huang, C. L., and Zhang, L. P.: Monitoring snow cover variability (2000-2014) in the Hengduan Mountains based on cloud-removed MODIS products with an adaptive spatio-temporal weighted method, J.
445 Hydrol., 551, 314-327, https://doi.org/10.1016/j.jhydrol.2017.05.049, 2017.

Li, X. H., Jing, Y. H., Shen, H. F., and Zhang, L. P.: The recent developments in cloud removal approaches of MODIS snow cover product, Hydrol. Earth Syst. Sci., 23, 2401-2416, https://doi.org/10.5194/hess-23-2401-2019, 2019.

Liang, H., Huang, X. D., Sun, Y. H., Wang, Y. L., and Liang, T. G.: Fractional Snow-Cover Mapping Based on MODIS and UAV Data over the Tibetan Plateau, Remote Sensing, 9, 1332, https://doi.org/10.3390/rs9121332, 2017.

450 Malmros, J. K., Mernild, S. H., Wilson, R., Tagesson, T., and Fensholt, R.: Snow cover and snow-albedo changes in the central Andes of Chile and Argentina from daily MODIS observations (2000-2016), Remote Sens. Environ., 209, 240-252, https://doi.org/10.1016/j.rse.2018.02.072, 2018.

Moosavi, V., Malekinezhad, H., and Shirmohammadi, B.: Fractional snow cover mapping from MODIS data using wavelet-artificial intelligence hybrid models, J. Hydrol., 511, 160-170, https://doi.org/10.1016/j.jhydrol.2014.01.015, 2014.

455 Pachauri, R. K., and Meyer, L.: Climate Change 2014: Synthesis Report. Contribution of Working Groups I, II and III to the Fifth Assessment Report of the Intergovernmental Panel on Climate Change, Climate Change 2014: Synthesis Report, 2014.

Parajka, J., and Bloschl, G.: Spatio-temporal combination of MODIS images - potential for snow cover mapping, Water Resour. Res., 44, W03406, https://doi.org/10.1029/2007wr006204, 2008.

Parajka, J., Pepe, M., Rampini, A., Rossi, S., and Bloschl, G.: A regional snow-line method for estimating snow cover from
460 MODIS during cloud cover, J. Hydrol., 381, 203-212, https://doi.org/10.1016/j.jhydrol.2009.11.042, 2010.

Riggs, G. A., and Hall, D. K.: MODIS Snow Products Collection 6 User Guide, 2015.

Riggs, G. A., Hall, D. K., and Roman, M. O.: Overview of NASA's MODIS and Visible Infrared Imaging Radiometer Suite (VIIRS) snow-cover Earth System Data Records, Earth Syst. Sci. Data, 9, 765-777, https://doi.org/10.5194/essd-9-765-2017, 2017.

465 Tang, Z. G., Wang, J., Li, H. Y., and Yan, L. L.: Spatiotemporal changes of snow cover over the Tibetan plateau based on cloud-removed moderate resolution imaging spectroradiometer fractional snow cover product from 2001 to 2011, J. Appl. Remote Sens., 7, 073582, https://doi.org/10.1117/1.jrs.7.073582, 2013.

Tong, R., Parajka, J., Komma, J., and Blöschl, G.: Mapping snow cover from daily Collection 6 MODIS products over Austria, J. Hydrol., 590, 125548, https://doi.org/10.1016/j.jhydrol.2020.125548, 2020.

470 Wang, J., Che, T., Li, Z., Li, H., Hao, X., Zheng, Z., Xiao, P., Li, X., Huang, X., and Zhong, X.: Investigation on Snow Characteristics and Their Distribution in China, Advances in Earth Science, 33, 12-16, https://doi.org/10.11867/j.issn.1001-8166.2018.01.0012, 2018.

Wang, X. W., Xie, H. J., and Liang, T. G.: Evaluation of MODIS snow cover and cloud mask and its application in Northern Xinjiang, China, Remote Sens. Environ., 112, 1497-1513, https://doi.org/10.1016/j.rse.2007.05.016, 2008.

475 Yu, J. Y., Zhang, G. Q., Yao, T. D., Xie, H. J., Zhang, H. B., Ke, C. Q., and Yao, R. Z.: Developing Daily Cloud-Free Snow Composite Products From MODIS Terra-Aqua and IMS for the Tibetan Plateau, IEEE Trans. Geosci. Remote Sens., 54, 2171-2180, https://doi.org/10.1109/tgrs.2015.2496950, 2016.

Yuan, Q., Shen, H., Li, T., Li, Z., Li, S., Jiang, Y., Xu, H., Tan, W., Yang, Q., Wang, J., Gao, J., and Zhang, L.: Deep learning in environmental remote sensing: Achievements and challenges, Remote Sens. Environ., 241, 111716,

480   https://doi.org/10.1016/j.rse.2020.111716, 2020.

Zhang, G., Xie, H., Yao, T., Liang, T., and Kang, S.: Snow cover dynamics of four lake basins over Tibetan Plateau using time series MODIS data (2001-2010), Water Resour. Res., 48, W10529, https://doi.org/10.1029/2012WR011971, 2012.

Zhang, H., Zhang, F., Zhang, G., Che, T., Yan, W., Ye, M., and Ma, N.: Ground-based evaluation of MODIS snow cover product V6 across China: Implications for the selection of NDSI threshold, Sci. Total Environ., 651, 2712-2726,
485   https://doi.org/10.1016/j.scitotenv.2018.10.128, 2019.

Zhang, H., Zhang, F., Zhang, G., Yan, W., and Li, S.: Enhanced scaling effects significantly lower the ability of MODIS normalized difference snow index to estimate fractional and binary snow cover on the Tibetan Plateau, J. Hydrol., 592, 125795, https://doi.org/10.1016/j.jhydrol.2020.125795, 2021.

Appendix A
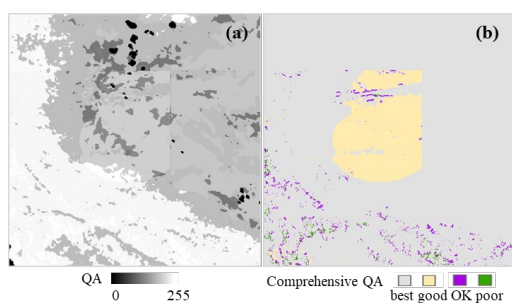
Figure A1. QA maps over Taklimakan Desert on 19 January 2008. (a) QA map. (b) Comprehensive QA map.
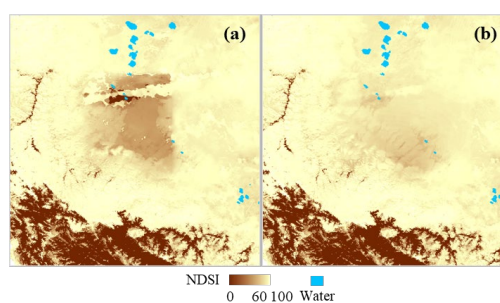
Figure A2. Post-processing over Taklimakan Desert on 19 January 2008. (a) STAR result. (b) Final result.

490
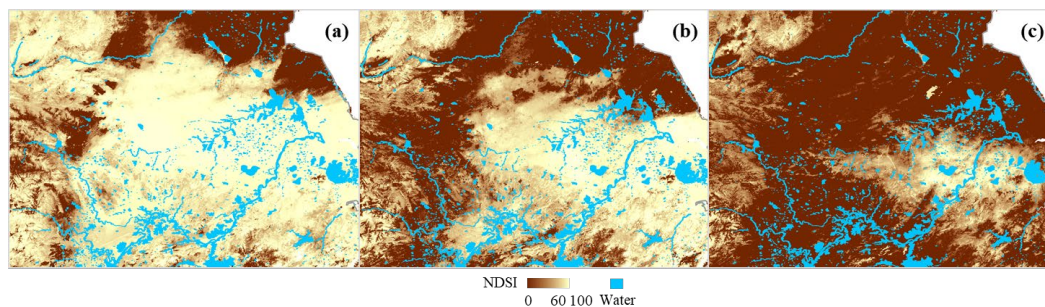
Figure A3. Extreme snow event in southern China. (a) 31 January 2008. (b) 5 February 2008. (c) 10 February 2008.